Mechanisms of Intense Alpine Rainfall

RICHARD ROTUNNO

National Center for Atmospheric Research, Boulder, Colorado

ROSSELLA FERRETTI

Department of Physics, University of L'Aquila, Coppito-L'Aquila, Italy

(Manuscript received 17 July 2000, in final form 25 October 2000)

ABSTRACT

Numerical studies by the authors and others of the 1994 Piedmont flood show that the orographically modified flow was a critical element for the production of extraordinary rainfall. To uncover the precise mechanism of orographic rainfall occurring in full-physics MM5 simulations of the 1994 Piedmont flood, the authors carried out simulations with the same real-data initial and boundary conditions, but with the real orography replaced by an idealized one. With excellent agreement between real and idealized orography on the rainfall rate versus time in the Piedmont area, analysis of the idealized-orography simulation provides a clear picture of the model's mechanism of orographically induced rainfall. As noted in previous studies of the 1994 Piedmont case, a moist saturated airflow has a reduced effective static stability and tends to flow over the mountains, while an unsaturated airstream is stable and tries to flow around (toward the left in the Northern Hemisphere). In the 1994 Piedmont case, there was a strong horizontal gradient of moisture; thus the western moist part of the airstream flows over, while the eastern drier part is deflected westward around the obstacle, and so a convergence is produced between the airstreams. This effect is explored using a simple version of MM5 wherein the flow, moisture distribution, and idealized orography are varied within the observed range. Quantitative as well as qualitative rainfall rates and flow features of the full-physics MM5 simulations are captured with the simple model.

1. Introduction

Numerical studies of the 1994 Piedmont flood show that the orographically modified flow was a critical element for the production of extraordinary rainfall (Romero et al. 1998; Buzzi et al. 1998; Ferretti et al. 2000). Orographically modified flow has two important effects on the total rainfall: first, the vertical motion has a major influence on the local rain rate, and second, the horizontal motion helps determine where and for how long the rain falls. Orographically modified flow is determined by the environmental static stability, Coriolis effect, and air velocity, and by the height, breadth, and shape of the orography. The complexity of Alpine orography (Fig. 1) and environmental flow (e.g., fronts, moisture, etc.) motivates the present study in which we attempt to improve the understanding of the mechanisms of intense Alpine rainfall through the use of progressively simpler representations of these factors in numerical simulations.

Given the ample documentation (Binder et al. 1996) and study (Doswell et al. 1998, and above references) of the 1994 Piedmont flood, our strategy is to use this case as the starting point for deeper analysis. As an introduction to the 1994 Piedmont case, consider Fig. 2, which contains a time sequence from a numerical simulation (details given below) of the weather over Europe on 5 November 1994 of the near-ground airflow and precipitable water during the most intense rainfall in Piedmont. Figure 2 shows an eastward-progressing tongue of moist southerly flow, rising over the approximately east–west Alpine barrier. Closer inspection of the Alpine southside reveals a significant westward deflection of the southerly flow by the east–west portion of Alpine barrier into a cul-de-sac (i.e., Piedmont) formed where the latter barrier turns to the north–south direction.

Sensitivity experiments by Buzzi et al. (1998) and Ferretti et al. (2000, hereafter FLR) show that when latent heating is suppressed, the southerly flow is deflected westward entirely around the Maritime Alps and Apennines (Fig. 1), and that therefore latent heating is required for rising motion and rainfall over Piedmont. On the other hand, Fig. 2 suggests, and FLR speculate,

* The National Center for Atmospheric Research is sponsored by the National Science Foundation.

Corresponding author address: Richard Rotunno, NCAR/MMM, P.O. Box 3000, Boulder, CO 80307-3000.
E-mail: rotunno@ucar.edu

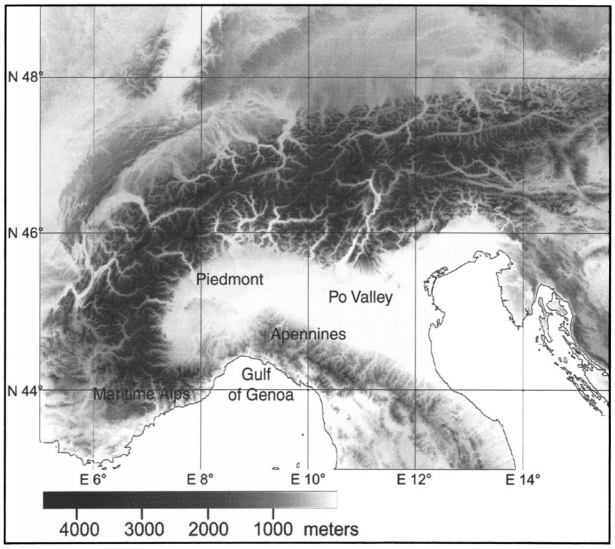

FIG. 1. Topographic map of the Alps with frequently mentioned geographical references.

that some westward deflection is necessary to explain the Piedmont-flood-producing flow. This need for an orographically modified flow with both ''flow-over'' and ''flow-around'' aspects motivated our experimental-design philosophy, which we now describe.

The first step involves isolating the effects of orographic shape within the context of the observed large-scale flow. Toward this end, numerical simulations were performed with the same real-data initial and boundary conditions as used in the simulation shown in Fig. 2, but with the actual orography replaced by an idealized lower boundary (based on an ''L'' shape rotated clockwise 90°). The excellent quantitative agreement between actual- and idealized-orography simulations on the rain rate versus time in the Piedmont region then allows analysis of the simpler model's mechanisms for intense Alpine rainfall. That analysis indicates the primary importance of the horizontal gradient in saturation deficit, which allows the almost saturated moist-adiabatic air of the moist tongue (see Fig. 2b) to flow over the Alpine barrier while the subsaturated air farther east is deflected westward; this pattern of horizontal motion effects not only the location of the rainfall but also the rain rate, as there is convergence between the more- and less-deflected airstreams.

The relative simplicity of the foregoing idea motivates further numerical experiments using not only idealized orography but also idealized environmental flow. Experiments varying the environmental flow and cross-stream moisture distribution within the observed range, together with experiments investigating aspects of orographic shape, capture quantitative as well as qualitative features of the rainfall occurring in the full-physics simulations.

The plan of the present paper is as follows. First, we review briefly in section 2 the observations of rainfall

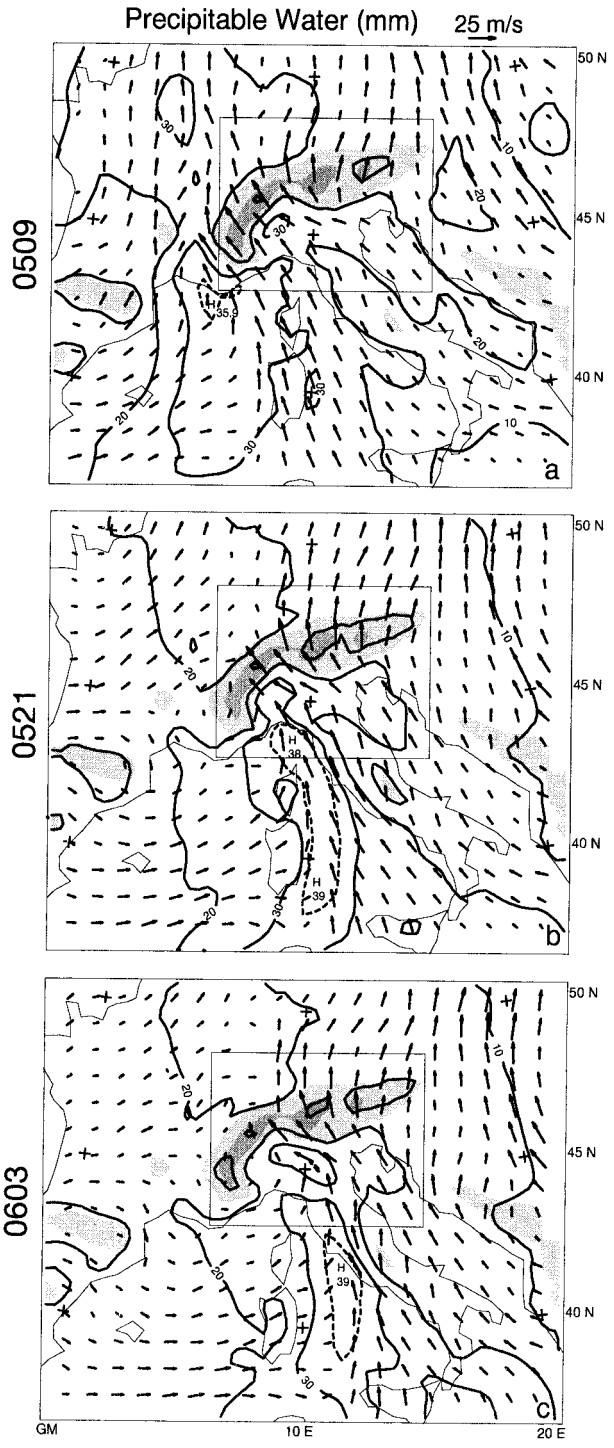

FIG. 2. Precipitable water (mm) and horizontal velocity vectors (displayed every five grid intervals) at $\sigma = 0.91$ (nearly terrain following) at (a) 0900 UTC 5 Nov 1994 (0509), (b) 2100 UTC 5 Nov 1994 (0521), and (c) 0300 UTC 6 Nov 1994 (0603) from a numerical simulation of the weather over Europe during the 1994 Piedmont flood. (The abbreviation for date and time will be used on this and all subsequent figures.) Here and for all subsequent figures light and dark shading indicates, respectively, elevations greater than 1000 and 2000 m. The inner box indicates the high-resolution subdomain.

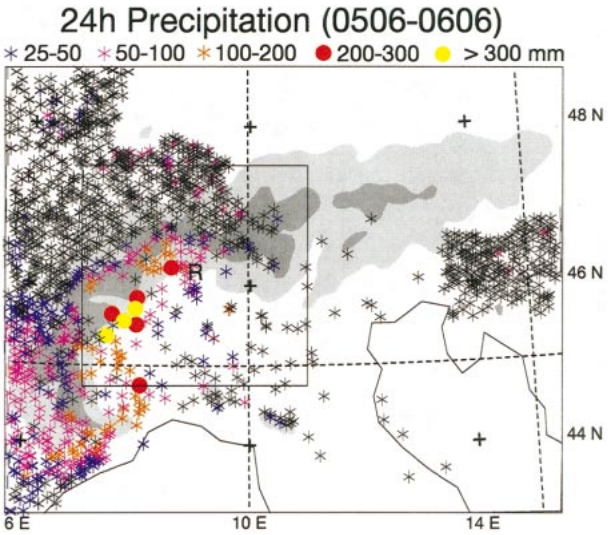

FIG. 3. Observed accumulated precipitation (mm) over the 24-h period ending 0600 UTC 6 Nov 1994 (0505–0606) on the small domain indicated in Fig. 2. Black crosses indicate rain gauges measuring less than 25 mm. Scan domain and position of the Monte Lema radar indicated by box with the R at the center.

for the 1994 Piedmont case. Section 3 contains an analysis of full-physics numerical simulations of the 1994 Piedmont case using idealized orography. We recall in section 4 aspects of the theory of orographic rain that can be used to provide a qualitative explanation of the simulations. These qualitative explanations are put to a quantitative test in section 5 using numerical simulations with both idealized orography and environmental flow. Section 6 contains a summary and outlook.

2. Rainfall observations

Figure 3 shows the observed rainfall for the 24-h period ending 0600 UTC 6 November 1994 within the area indicated in Fig. 2. The rainfall leading to the Piedmont flood occurred along the steep southeastward-facing slopes of the Alps (between 45° and 46°N), with amounts in excess of 300 mm observed. These amounts are in addition to accumulations in excess of 100 mm observed at the same stations in the preceding 24-h period (see Fig. 5a of FLR). Generally speaking, the largest accumulations of rain were on the windward slopes, however Buzzi et al. (1998) point out that large amounts occurred leeward of the Maritime Alps (Fig. 1), as one can see in Fig. 3 (near 44.8°N, 8°E).

To obtain a closer look at the rainfall over time, we examined the best estimate of radar-derived precipitation rate from the Monte Lema radar (Joss et al. 1998; location indicated by the ''R'' in Fig. 3) at 5-min intervals (available online at http://www.map.ethz.ch). The time sequence (not shown) begins at 1530 UTC 4 November 1994 and indicates motion generally from the SSE, consistent with the observed 850-mb flow (Fig. 3 of FLR). Figure 4a (0900 UTC 5 November 1994) is

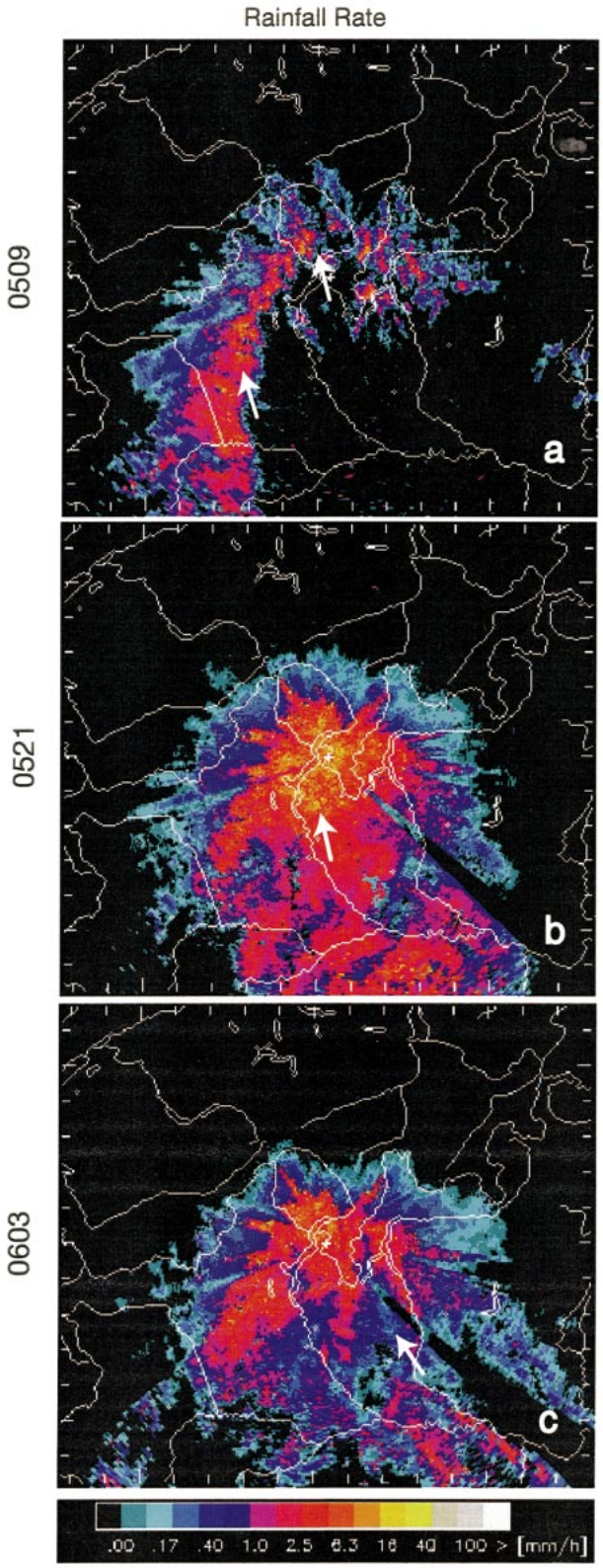

FIG. 4. Best estimate of radar-derived precipitation rate from the Monte Lema radar on the domain indicated in Fig. 2 at (a) 0900 UTC 5 Nov 1994, (b) 2100 UTC 5 Nov 1994, and (c) 0300 UTC 6 Nov 1994. These images are obtainable on the Web at http://www.map.ethz.ch, but note we have changed the color scale for greater clarity.

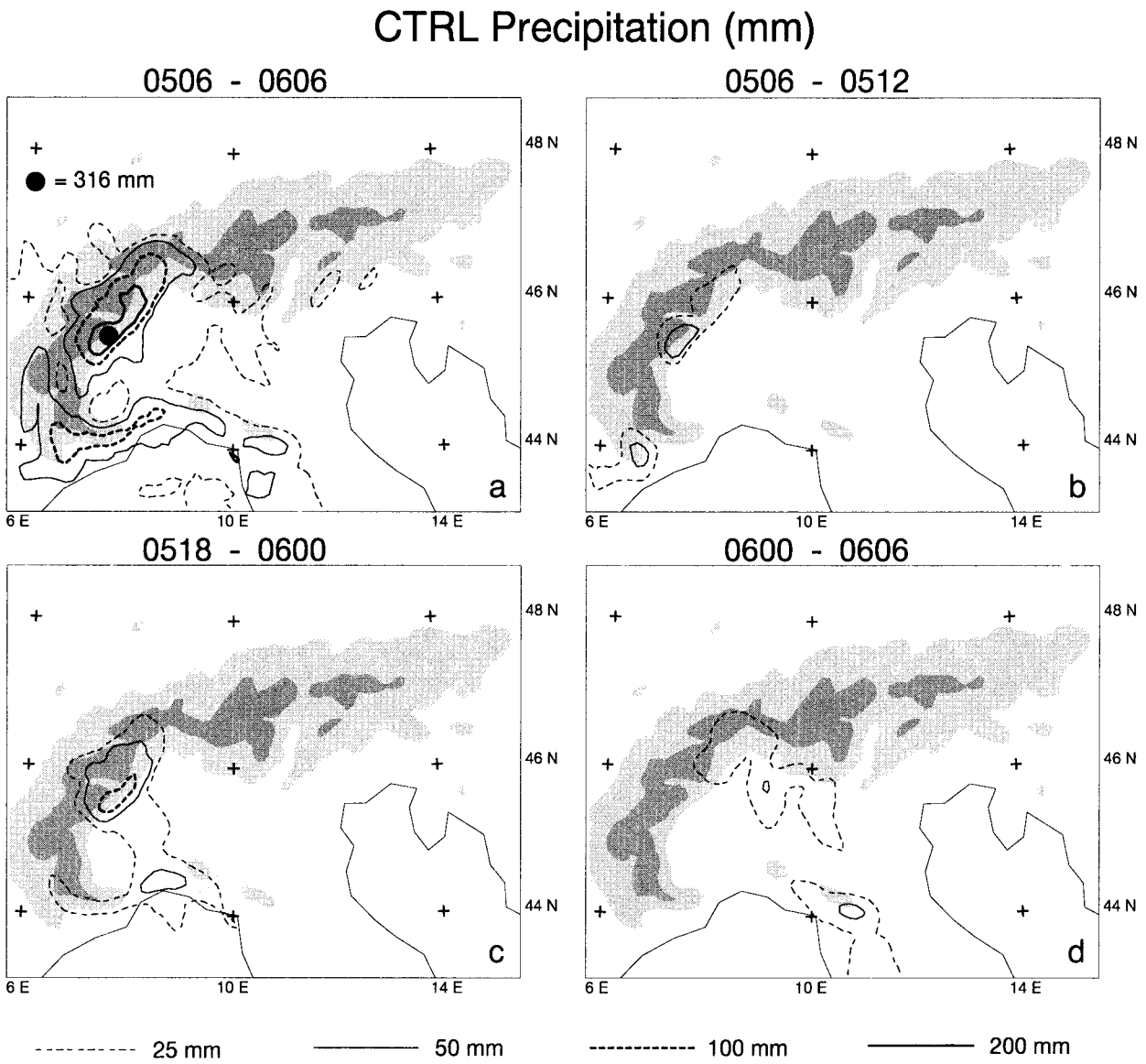

FIG. 5. Accumulated precipitation (mm) from an MM5 simulation (CTRL) of the weather during the 1994 Piedmont flood for the (a) 24-h period ending 0600 UTC 6 Nov 1994, (b) 6-h period ending 1200 UTC 5 Nov 1994, (c) 6-h period ending 0000 UTC 6 Nov 1994, and (d) 6-h period ending 0600 UTC 6 Nov 1994.

roughly representative of those of the previous 17.5-h; the rainfall is concentrated along the eastward and southeastward-facing slopes of the western Alps, with maximum intensities ranging from 2.5 to 8.3 mm h^{-1}. The distribution and intensity of the rain rate is broadly consistent with the greater than 100 mm of rain observed in the earlier 24-h period ending 0600 UTC 5 November 1994 (Fig. 5a of FLR). Beginning around 1800 UTC 5 November 1994, the time sequence shows that the areal coverage and peak values of rain rate increase and begin to migrate eastward. Figure 4b (2100 UTC 5 November 1994) shows that in the latter part of the 24-h period ending 0600 UTC 6 November 1994 (Fig. 3) there is a major increase in rain rate to somewhere in the range 8.3 to greater than 18 mm h^{-1} that lasts approximately 6 h. Later, Fig. 4c (0300 UTC 6 November 1994) indicates still large, but weakening rain rates in the vicinity of the radar location. Our subjective analysis of the image time sequence indicates motion backing from SSE to SE (white arrows in Fig. 4).

3. Simulations with idealized orography

a. The control run

The basic setup for the numerical experiments presented here was described in FLR, and so only the most essential information will be repeated here. The nu-

merical model used is the Pennsylvania State University–National Center for Atmospheric Research (PSU–NCAR), mesoscale model (MM5; Dudhia 1993). The computational domain (Fig. 2) has 51×61 grid points in the north–south and east–west directions, respectively, with a horizontal grid spacing of 30 km. All the simulations in this section use the same initial and boundary conditions, which are derived from the European Centre for Medium-Range Weather Forecasts (ECMWF) global data analyses with 0.5° resolution. The 6-h ECMWF analyses are interpolated to MM5 lambert conformal grids to provide both the initial condition at 1200 UTC 4 November 1994, and the 6-h lateral boundary conditions to the 30-km domain. Within this coarse-mesh domain, a two-way interactive 10-km grid is embedded and centered over the Alps (inner box in Fig. 2, shifted to the east with respect to the simulations reported in FLR) to resolve more accurately the complex orographic flow in this region. In the vertical, the model has 24 unevenly spaced layers with more levels being placed in the boundary layer; the lowest model level is approximately 40 m above the ground. The simulations reported here use the cumulus parameterization of Kain and Fritsch (1993) and the bulk planetary boundary layer parameterization of Troen and Mahrt (1986). The simulation using all these features is called the control run (designated CTRL).

It was shown in FLR that their MM5 simulation captured the amount and location of the heavy rain observed in the 1994 Piedmont flood. Figure 5a shows that the CTRL simulated fine-grid (box indicated in Fig. 2) rainfall for the 24-h period ending 0600 UTC 6 November 1994 compares similarly well with the observations shown in Fig. 3.

As with the observations reported in the previous section, we have examined the rain rate in subintervals of the period ending 0600 UTC 6 November 1994. During the first 6-h interval (0506–0512, Fig. 5b), the peak accumulations are around 60 mm, and are located on the steep windward slopes of the Maritime Alps and the Alps near Piedmont. Hence the average rain rate is approximately 10 mm h^{-1}. The next 6-h interval (0512–0518) is very similar to the previous, and is therefore not shown. During the next 6 h interval (0518–0600, Fig. 5c), there is a major change in intensity and distribution of the rainfall. Along with the eastward movement of the southerly inflow (Fig. 2), the rainfall pattern windward of the Maritime Alps shifts eastward. However, rain continues in Piedmont, falling at an average rate of over 20 mm h^{-1}. Note there is a zone of moderate 6-h accumulation (>25 mm) running from the Gulf of Genoa NNW to Piedmont. During the last 6-h (0600–0606, Fig. 5d), moderate-to-heavy accumulations are moving eastward, more or less in step with the movement of the large-scale pattern (Fig. 2). Comparing the radar estimates of rainfall rate (Figs. 4a–c) with the model prediction (Figs. 5b–d) shows a general agreement in the precipitation evolution. Earlier the rain rate is weaker and confined to the windward slopes, while later there is essentially a doubling of the rain rate, with significant rainfall upwind of the steepest slopes.

b. Ideal Alps

The complexity of the Alpine orography is a significant impediment to interpretation. Hence as a first step toward explanation, simulations were performed that were identical to the control (CTRL), except for the use of simplified representations of the Alps. Following Schneidereit and Schär (2000), we use the orography described by the function

$$h(x, y) = H \cos^2 \frac{\pi |l(x, y)|}{2L}, \tag{3.1}$$

where $|l(x, y)|$ is the shortest geometrical distance between the point (x, y) and the ridge line, which defines the shape of the obstacle in the $x - y$ plane. As in Schneidereit and Schär (2000), we consider two shapes (although with different parameter settings): one has an east–west ridge line defined by -240 km $< x < +240$ km at $y = 0$; the other has an east–west ridge line, -120 km $< x < +240$ km at $y = 0$, joined by a quarter-circle ridge line of radius 120 km and centered at $(-120, -120)$ km, which in turn is joined by the north–south ridge line, -240 km $< y < -120$ km at $x = -240$ km. The maximum height $H = 2500$ m for all simulations; L is the shortest horizontal distance between a point on the ridge line and the place where $h = 0$; in the simulations to be described next (designated ideal Alps), $L = 60$ km, roughly corresponding to the steepest slopes of the Alpine southside (which are in Piedmont).

The 24-h rainfall (Fig. 6a) from the ideal Alps simulation shows that rain along the coastal mountains of the Gulf of Genoa (Fig. 5a) is now gone; however, the rainfall in the idealized Piedmont remains, and is quantitatively, as well as qualitatively, similar to that of CTRL. Furthermore, the time dependence of the 6-h accumulations (Figs. 6b–d) exhibit an excellent correspondence to those in CTRL (Figs. 5b–d) with respect to the rain in Piedmont. This level of agreement means that we can profitably examine the mechanisms of intense Alpine rainfall with the simpler model configuration.

The flow that produces the rain in the periods shown in Figs. 6b–d is shown in Fig. 7, which contains the horizontal velocity vectors and the equivalent potential temperature θ_e at the nearly terrain-following level $\sigma = 0.97$ (left column) and at the just-above-mountain pressure level $P = 700$ mb (right column) on the inner domain of the ideal Alps simulation. (The near-Alps flow on the outer domain does not differ significantly from that shown in Fig. 2 for CTRL.) Early in the period (0509), when the rain rate is roughly 10 mm h^{-1}, Fig. 7a shows that at low levels, the flow of higher-θ_e air from the SSE is met by lower-θ_e air flowing along the east–west portion of the barrier; above the mountain,

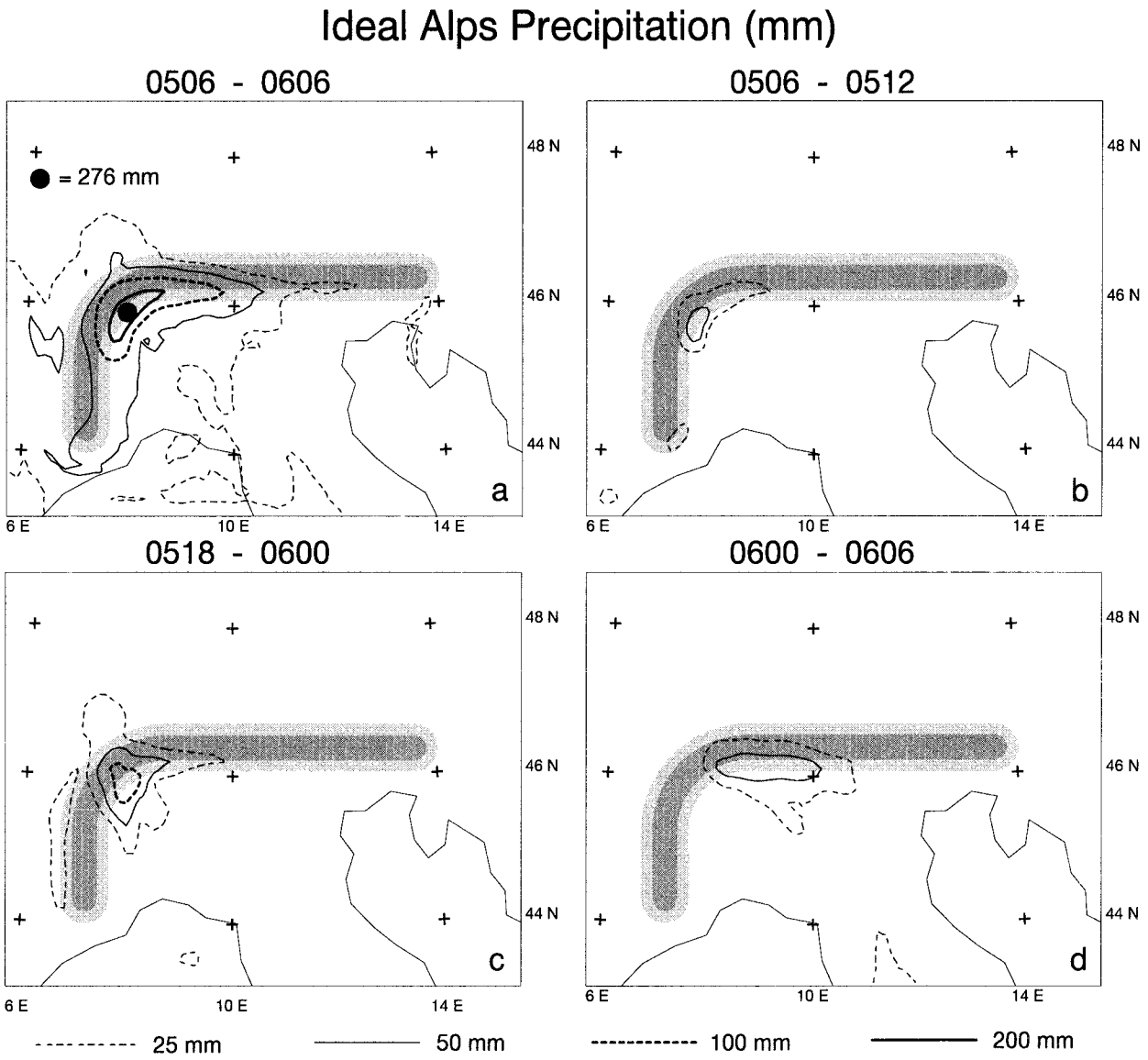

FIG. 6. As in Fig. 5 except for the ideal Alps simulation.

Fig. 7b shows roughly 10 m s^{-1} SSE flow of higher-θ_e air in the west and lower-θ_e air in the east. Later in the period (0521), when the rain rate is roughly 20 mm h^{-1}, Fig. 7c shows an intensification of both the southerly flow from the Gulf of Genoa, and the easterly along-barrier flow; above the mountain, Fig. 7d shows an intensification of the southerly flow to roughly 15 m s^{-1} along with a stronger east–west gradient of θ_e over the idealized Po Valley. It is significant that, at this time of heaviest rain, the cold front (indicated by the strong θ_e gradient, near 7°E in Fig. 7c) is only just entering the inner domain. The lack of a direct connection between the cold front and the area of heavy rain is even more evident at 0603 (Fig. 7e), when the cold front stalled on the west side of the north–south ''leg'' of the idealized Alps[1]; Figs. 7e–f, together with Fig. 6d, show that the most intense rain continues to fall where the higher-θ_e southerly flow meets the lower-θ_e along-barrier easterly flow.

The flow in the ideal Alps simulation is further examined in the vertical cross sections indicated by the lines A - A' in Figs. 7b, 7d, and 7f. These lines go through the maximum 6-h accumulated rain for the intervals displayed in Figs. 6b, 6c, and 6d, respectively; the orientation of the lines A - A' is chosen to be roughly along the local low-level flow direction indicated in Figs. 7b and 7d, and the orientation in Fig. 7f is chosen

[1] Retardation by the Alps of a cold front's eastward progress is a commonly observed feature (e.g., Steinacker 1981).

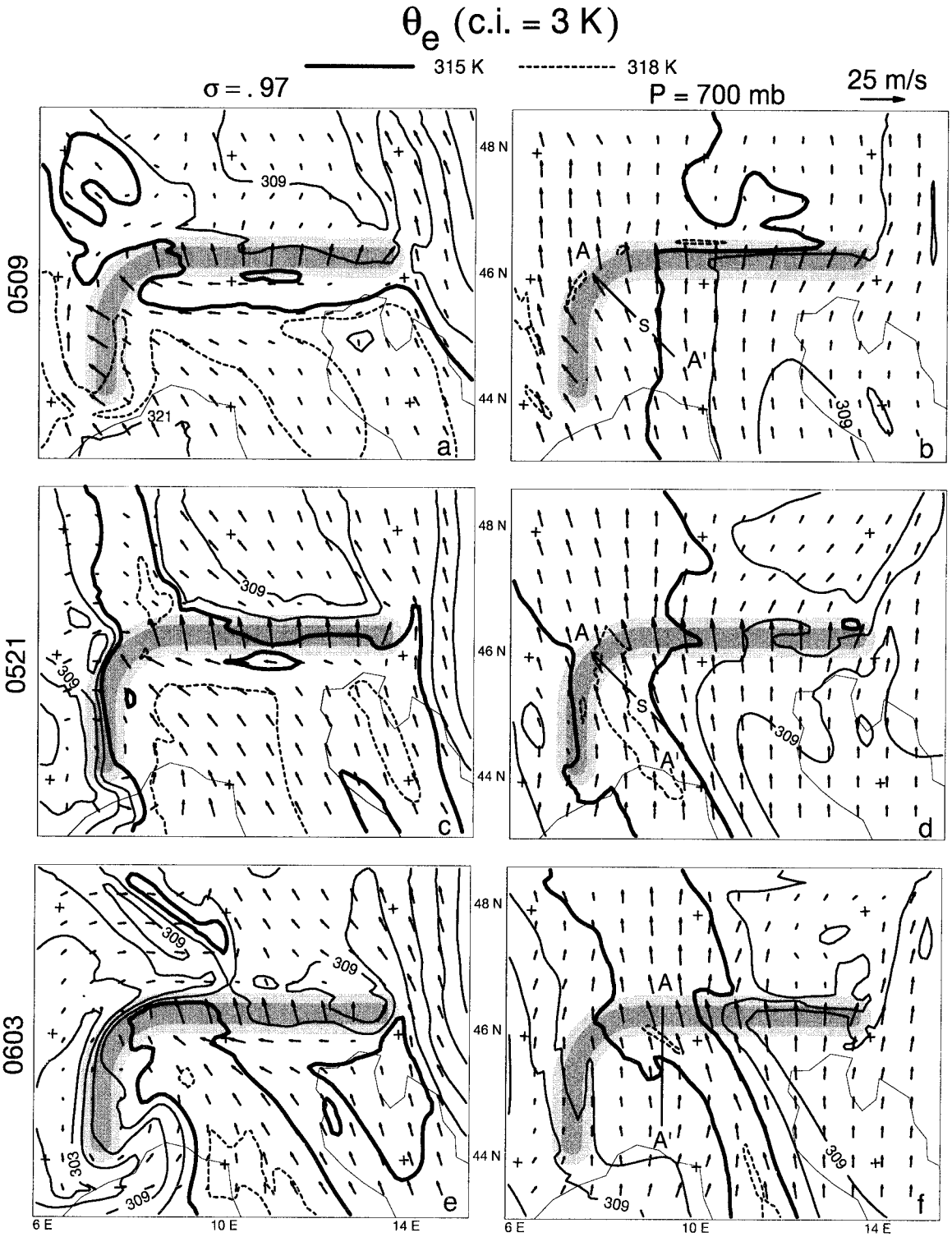

FIG. 7. Equivalent potential temperature θ_e and horizontal velocity vectors (displayed every five grid intervals) (left) at $\sigma = 0.97$ and (right) $P = 700$ mb from the ideal Alps simulation at (first row) 0900 UTC 5 Nov 1994, (second row) 2100 UTC 5 Nov 1994, and (last row) 0300 UTC 6 Nov 1994. Lines *A*–*A*′ indicate the positions of the vertical cross sections shown in Figs. 8a–c and the S symbols denote the positions of the soundings shown in Figs. 9a,b.

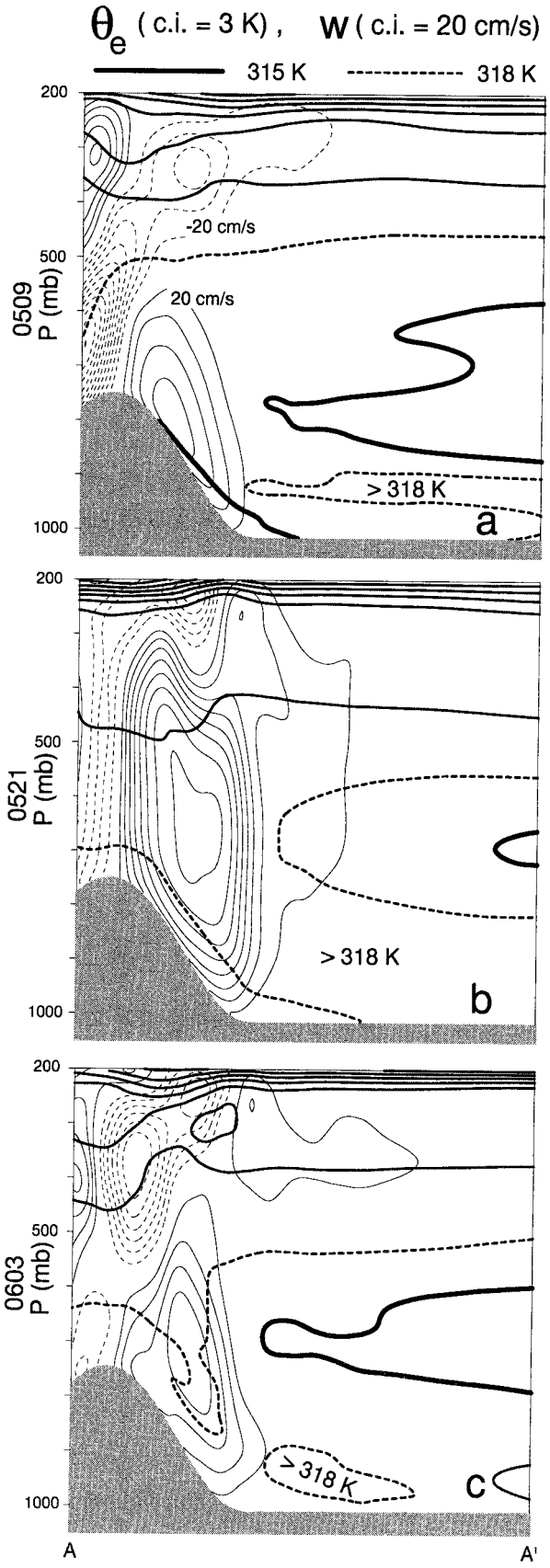

FIG. 8. Vertical cross sections of θ_e and vertical velocity w from the ideal Alps simulation at (a) 0900 UTC 5 Nov 1994 (A–A' in Fig. 7b), (b) 2100 UTC 5 Nov 1994 (A–A' in Fig. 7d), and (c) 0300 UTC 6 Nov 1994 (A–A' in Fig. 7f).

to be north–south. Figure 8 shows the vertical component of velocity w, and θ_e in these vertical cross sections. At the earlier stage of less-intense rainfall (0509, Fig. 8a), w has a maximum value located slightly above the steep windward slope; the θ_e field shows a current defined by $\theta_e > 315$ K rising over the barrier; there is a blanket of lower-θ_e air on the windward slope that is due to the eastward along-barrier flow (Fig. 7a). At the later time of more intense rainfall (0521, Fig. 8b), the maximum value of w has more than doubled, and is now located near $P = 700$ mb, indicating strong convergence just above the windward slope; the structure of the θ_e field is similar to that of the earlier period (Fig. 8a). At the last time of the sequence (0603), Fig. 8c shows that the maximum w continues to be located above the low-θ_e air that blankets the windward slope. The soundings (Fig. 9) taken just upstream of the vertical velocity maxima (marked by the ''S'' in Figs. 7b and 7d) show that the air is nearly conditionally stable, and hence the mid-level maximum of w, seen in Fig. 8b, is not due to moist convective instability, explicit or parameterized.

The foregoing analysis of the airflow in the ideal Alps simulation suggests two distinct regimes of orographic flow corresponding to two distinctly different regimes of rainfall distribution and intensity. In one regime (Fig. 8a), the flow is forced upward by the mountain and so the maximum w is at the surface on the windward slope. In the other regime (Figs. 8b,c), w is strongly influenced by the convergence of higher-θ_e southerly flow with lower-θ_e along barrier easterly flow. In both cases the vertical motion is due to orographic-flow modification, however in the sense to be described in sections 4–5, the orographic response of w is direct in the first regime and indirect in the latter one. Analysis of CTRL (not shown) leads to the same conclusion.

c. Other ideal Alps

Several additional experiments were carried out with the idealized orography (3.1) to help round out the picture. Figure 10a shows the 24-h rainfall from a simulation using the same orographic shape as in ideal Alps, but with $L = 120$ km (designated less steep). The 24-h rainfall is reduced in less steep to 240 from 276 mm in ideal Alps; this relatively slight 12% reduction suggests a subtle orographic effect as it implies that the rain rate is not directly proportional to the magnitude of the slope. Figure 10b shows the 24-h rainfall in a simulation with $L = 60$ km, as in ideal Alps, but with the north–south leg removed (designated no leg). The 24-h rainfall is now only 167 mm. There are two reasons

←

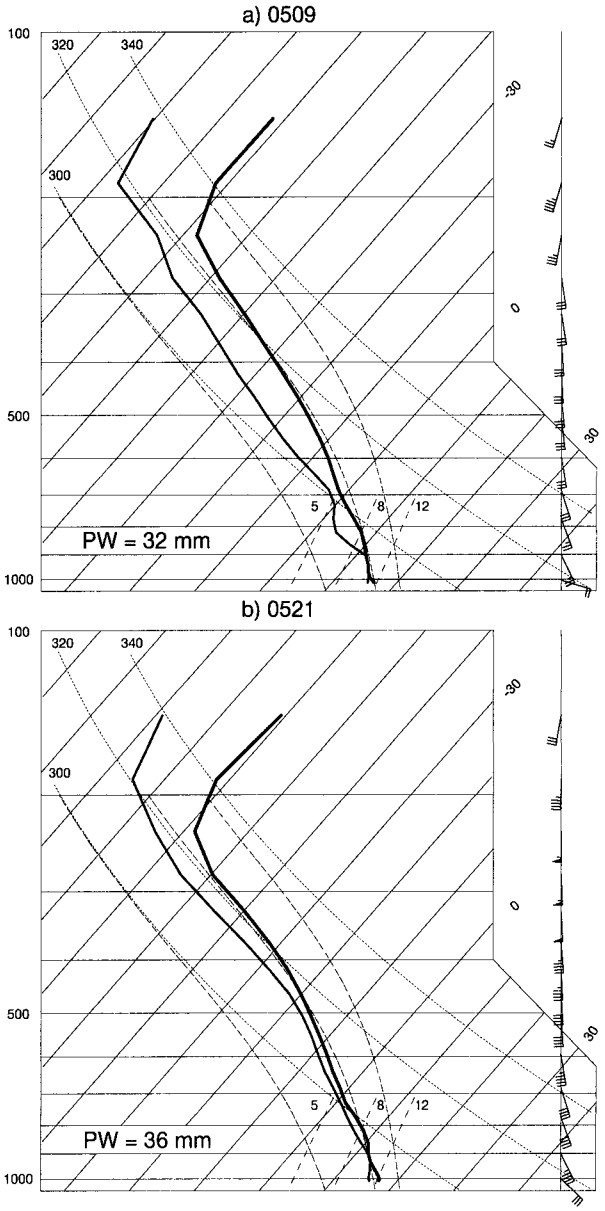

FIG. 9. Soundings displayed from the ideal Alps simulation at (a) 0900 UTC 5 Nov 1994 (S in Fig. 7b) and (b) 2100 UTC 5 Nov 1994 (S in Fig. 7d). Precipitable water in the column indicated by PW.

for this reduction: first, there is little rain in the early period of no leg when in ideal Alps there is significant rainfall due to SSE flow up the slopes of the leg (Figs. 6b and 7a). Second, although a rain rate of approximately 20 mm h^{-1} occurs in the later period (0521, not shown) of no leg [as it did in ideal Alps (Fig. 6c)], the absence of the leg allows the cold front (seen to be stalled in Fig. 7c) to sweep the system eastward rapidly and so there are smaller local accumulations. A fuller explanation of these simulations will be given within the theoretical framework established next.

4. Theoretical framework

The rainfall at a location is by definition the rain rate $R(t)$ integrated over the duration T, namely,

$$\mathcal{R} \equiv \int_0^T R(t)\, dt. \tag{4.1}$$

Although orographic control of R is by far the more difficult to understand, the orographic influence on T is equally important when trying to explain a flood. We consider each factor in turn.

a. Rain rate

Kessler (1969) gives the simplest set of equations containing the physics we believe relevant to the meteorology of the 1994 Piedmont flood. Water substance is considered in three categories: vapor, liquid moving with air (cloud water), and liquid descending vertically through air (rainwater). The mass per unit volume of dry air of each is denoted by ρ_v, ρ_c, ρ_r, respectively. Under saturated conditions (not very far from the truth in the present application; see also Fig. 9b), the equation for $\rho_c + \rho_r$ ($\equiv \rho_l$) is

$$\frac{d\rho_l}{dt} + (\rho_l + \rho_{vs})(\partial_x u + \partial_y v + \partial_z w) = -\frac{d\rho_{vs}}{dt} + \frac{\partial \rho_r V_r}{\partial z}, \tag{4.2}$$

where ρ_{vs} is the saturation vapor density and V_r (here positive by definition) is the mass-weighted-average raindrop fall speed relative to the air motion; $d/dt = u\partial_x + v\partial_y + w\partial_z$, and u, v, and w are the velocity components along the x (east–west), y (north–south), and z (vertical) directions, respectively.

To give a simple illustration of how orography exercises control over precipitation, Smith (1979, hereafter S79) considers a balance between the two terms on the rhs of (4.2). With the first term approximated by the vertical advection, integration of (4.2) over z from the ground level h to a height large enough for ρ_r to vanish, gives

$$R = \int_h^\infty - w\frac{\partial \rho_{vs}}{\partial z}\, dz, \tag{4.3}$$

where $R \equiv (\rho_r V_r)_{z=h}$ is the rain rate [cf. Eq. (4.4) of S79]. Equation (4.3) shows that R is directly proportional to the vertical motion of the assumed saturated airflow. S79 discusses the simplest possible model of orographic flow: $w = VH/L$, where V is constant denoting the speed of air directed at a two-dimensional barrier that rises to height H over a distance L. Since w is constant with height in this model, (4.3) yields immediately,

$$R = V\frac{H}{L}\rho_{vs}(h). \tag{4.4}$$

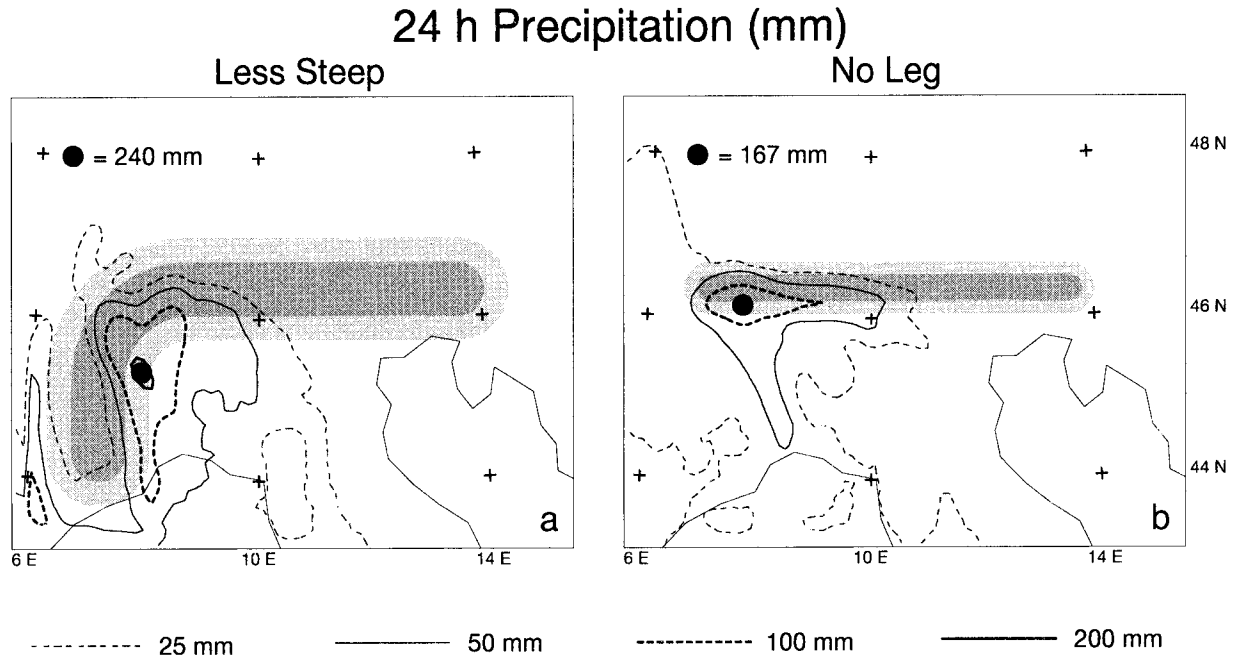

FIG. 10. As in Fig. 6a for ideal Alps except for simulations using idealized orography (a) with a slope half as great (less steep) and (b) without the north–south leg (no leg).

Using the typical values, $H/L = 0.01$, $V = 10$ m s^{-1}, and $\rho_{vs}(1000\text{ m}) \approx 0.01$ kg m^{-3}, (4.4) gives $R \approx 0.001$ mm s^{-1} = 3.6 mm h^{-1}, which is typical of observed orographic rain rates.

b. Rainfall duration

The duration $T \approx \lambda/U$, where λ and U are the horizontal scale and speed of a rain-producing synoptic-scale feature. For example, a rough estimate from Fig. 2 gives that the east–west scale of the moist tongue is approximately 500 km and moves eastward at around 5 m s^{-1}, hence $T \approx 1$ day. Also evident in Fig. 2, and in more detail in Fig. 7, is the fact that the orography locally induces an westward flow perturbation, which tends to reduce U locally, and so, increase T.

c. Theory

The major difficulty in developing a theory for R [even accepting the assumptions leading to (4.3)] and T is understanding orographic-flow modification including the effects of latent heating. The main analytical problem is due to the physical fact that latent heating only affects the dynamics when the air is saturated, and for any given problem, one does not know a priori the locations of saturated and unsaturated air (e.g., Barcilon et al. 1979). Thinking on the topic has been guided by extension of the theory for orographic-flow modification in the absence of latent heating, which we now briefly describe.

Consider a flow with speed V of a rotating, stratified fluid, characterized by the Coriolis parameter, f, and the Brunt–Väisälä frequency, N, respectively, past a mountain of height H and width L. From the parameters, V, N, and f, one can form two length scales, namely, V/N and V/f; for values typical of midlatitude conditions ($V = 10$ m s^{-1}, $N = 0.01$ s^{-1}, $f = 10^{-4}$ s^{-1}) these are, respectively, 1 and 100 km. For the mountains of Earth, H is at most 5 km, however L can be $O(1000)$ km. Given these essential geophysical facts, we organize the orographic-flow regime chart shown in Fig. 11 with logarithmic abscissa L and linear ordinate H. In judging mountain height H, the only geophysically relevant scale is V/N; experience shows that the dividing line between linear and nonlinear flow response is where $H \approx V/N$ (S79, p. 128). In judging mountain width L, both V/N and V/f are geophysically relevant scales. For $L < V/N$, nonhydrostatic effects are important. For $V/N < L < V/f$, the flow is hydrostatic and the effects of f may be neglected; the linear response comes in the form of mountain waves (Queney 1948) and the nonlinear response is characterized by upstream blocking and lee-side wave breaking for a two-dimensional ridge (e.g., Pierrehumbert and Wyman 1985) or by flow-splitting and lee-vortex formation for a three-dimensional obstacle (Smolarkiewicz and Rotunno 1989); for $L > V/f$, the flow is hydrostatic and rotation is a dominant influence; quasigeostrophic theory solutions (e.g., Buzzi and Tibaldi 1977; section 3.1 of S79) show an anticyclonic flow perturbation over weak orography ($H < fL/N$), which becomes a vortex with closed streamlines (e.g., Merkine and Kalnay-Rivas 1976) for strong orography ($H > fL/N$). Numerical solutions of the primitive equa-

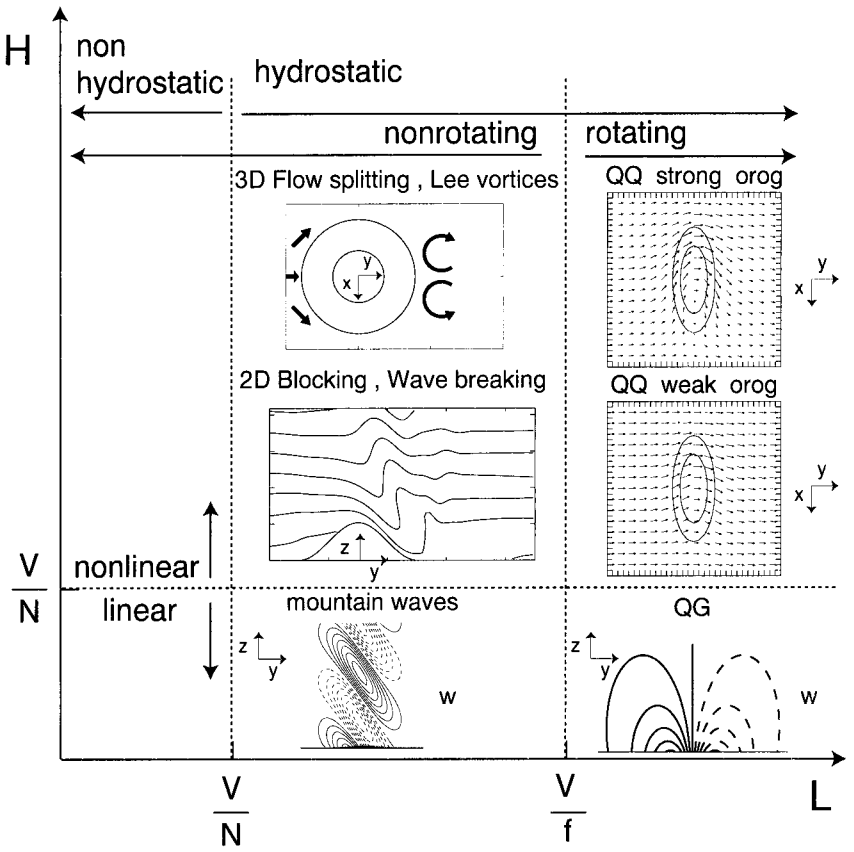

FIG. 11. Regime diagram for dry-adiabatic, constant flow (V) of a uniformly stratified (N = constant) fluid on an f plane past an obstacle of height H and breadth L. The diagram assumes typical Northern Hemisphere midlatitude values for N and f such that $N \gg f > 0$.

tions in the regime $H > V/N$ and $L \sim V/f$ are given in Trüb and Davies (1995) for flow past a two-dimensional ridge, and by Peng et al. (1995) for flow past three-dimensional obstacles.

The foregoing survey is by no means exhaustive as we have intentionally emphasized those parts of the regime diagram we believe relevant to the present application. Even the crudest estimate of H for the Alps (Fig. 1) puts the orographic-flow response in the nonlinear part of the regime diagram (Fig. 11). Particularly important for orographic rain is the nonlinear response on the windward side, which, as shown by the icons in Fig. 11, has flown around, rather than over, a three-dimensional obstacle. Estimating the relevant horizontal scale L is not as easy since there is a rich spectrum of horizontal scales (Fig. 1) each affecting different aspects of the flow. Restricting attention to flow features on the larger scale of the Alps puts L in the regime where the effects of rotation are important (Fig. 11). The primary effect of rotation is the leftward-deflection (in the Northern Hemisphere) of the split flow in the nonlinear regime (Fig. 11). An accompanying feature of the latter horizontal flow pattern is for the vertical velocity to be small on the right side (since the flow there is tending to follow height contours) and large on the left; the vertical motion is shown in Fig. 14 of Peng et al. (1995) from a primitive-equation numerical simulation of orograhically modified flow with $H = 4V/N$ and $L \approx 19.2V/f$. Numerical experiments in the same general range of L and H by Schneidereit and Schär (2000), using an obstacle with more uniform steepness (as in Fig. 10b), show a more complete leftward deflection of the air with little rising motion (see their Fig. 6), consistent with the sensitivity studies of Buzzi et al. (1998, their Fig. 12) and FLR (particularly their Fig. 12d).

The simulations presented in the previous section suggest the importance of convectively stable-to-neutral flow (see Fig. 9) in the orographic precipitation process. Although convectively neutral orographic flow is simpler than moist unstable orographic flow (see, e.g., S79, p. 193), the simplest case of a saturated moist-adiabatic atmosphere has $N = 0$, and direct application to Fig. 11 is still problematic. The authors are unaware of any study treating the case of saturated moist-adiabatic flow over a mountain barrier. The closest is that of Durran and Klemp (1983) in which numerical simulations of stably stratified dry and saturated air, respectively, flowing over a two-dimensional mountain (their Figs. 13–

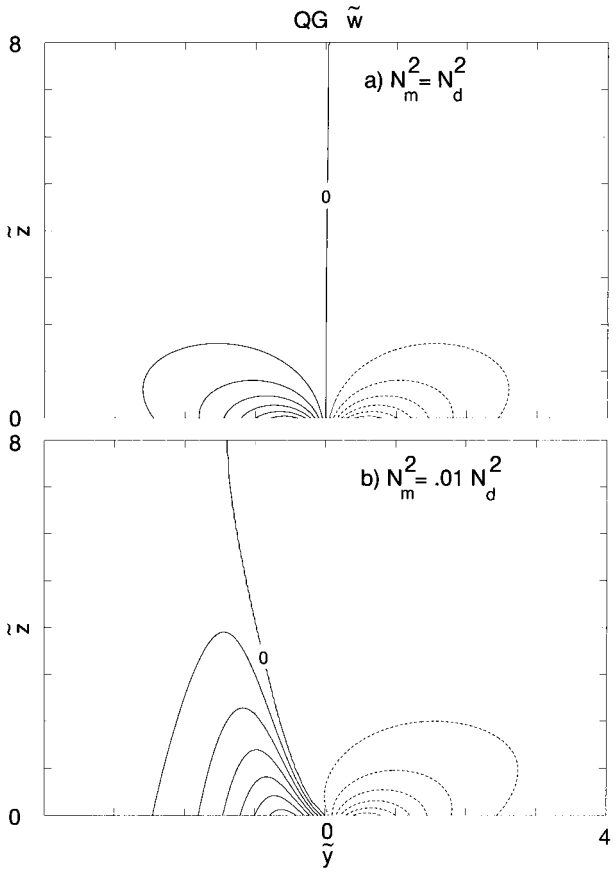

FIG. 12. Quasigeostrophic solution for nondimensional $\tilde{w} = Lw/VH$ for flow past a two-dimensional ridge for (a) uniform static stability in rising and sinking air and (b) small static stability where the air rises. Nondimensional coordinates $\tilde{y} = y/L$ and $\tilde{z} = N_d z/fL$.

15) in the nonrotating, hydrostatic regime are compared. The reduced static stability in the moist case has the effect of increasing the vertical scale of the mountain wave.

In a study of orographic cyclogenesis in a saturated atmosphere, Benzi et al. (1997) solved the quasigeostrophic equations developed by Fantini (1995) for a moist atmosphere. For the case of a two-dimensional ridge ($\partial_x = 0$), we notice that the solution of Fantini's (1995) equations requires only the solution of

$$(N^2 w)_{yy} + f^2 w_{zz} = 0, \tag{4.5}$$

with boundary conditions $w = Vh_y$ at $z = 0$ and $w = 0$ at $z = z_{\text{top}}$. The static stability varies according to

$$N^2 = \begin{cases} N_d^2 & w < 0 \\ N_m^2 & w > 0, \end{cases} \tag{4.6}$$

where N_d is the normal dry static stability and N_m is a reduced static stability that accounts for the effects of latent heating; the theory applies for $0 < N_m^2 < N_d^2$. With the simple bell-shaped orography,

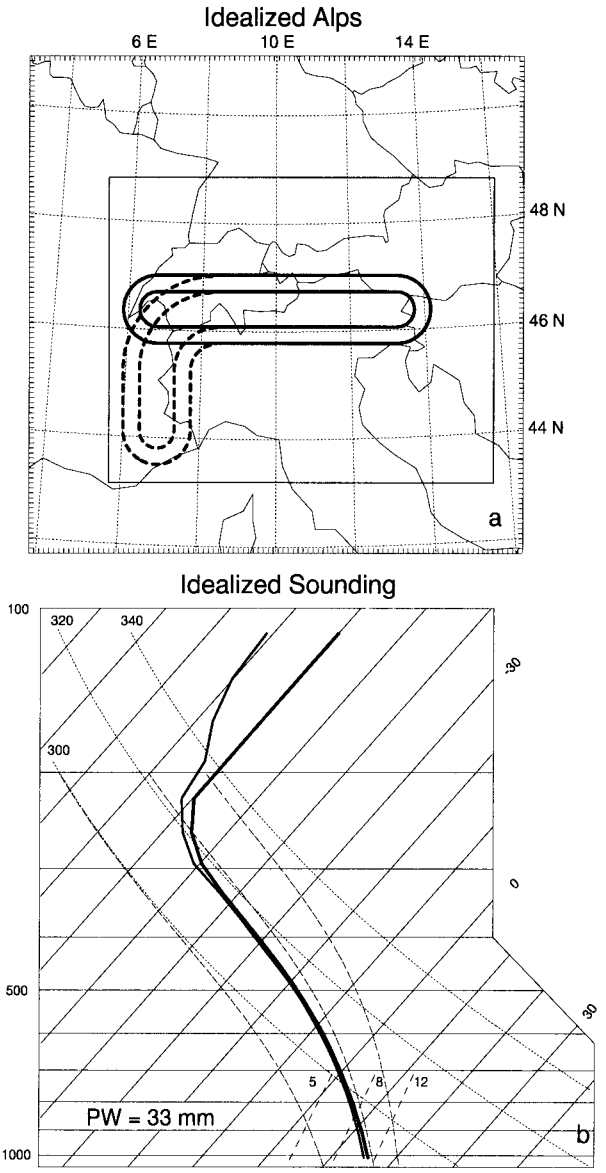

FIG. 13. (a) Domain and (b) initial sounding for MM5 simulations using idealized environmental flow and orography. The domain shown is 1000 km × 1000 km with tick marks indicating grid points with spacing 10 km. Two shapes of orography are used here: an east–west barrier (solid lines c.i. = 1000 m) and another with a north–south leg (dashed lines). The idealized sounding shown in (b) is used as a basis for further experiments on the effect of horizontal gradients of moisture. The inner box is the display domain for Figs. 14–15.

$$h(y) = \frac{HL^2}{y^2 + L^2}, \tag{4.7}$$

we solve (4.5)–(4.7) through successive overrelaxation on a domain $(y, z) \in (-4L, 4L) \times (0, 8fL/N_d)$ with resolution $ny \times nz = 320 \times 120$ for $N_m^2/N_d^2 = 0.01$ and 1, respectively. Figure 12 shows that even with $N_m \ll N_d$ the solutions are well-behaved, exhibiting only a larger decay scale on the upwind side. With weaker $|\partial_z w|$ in the rising motion in the moist case (Fig. 12b)

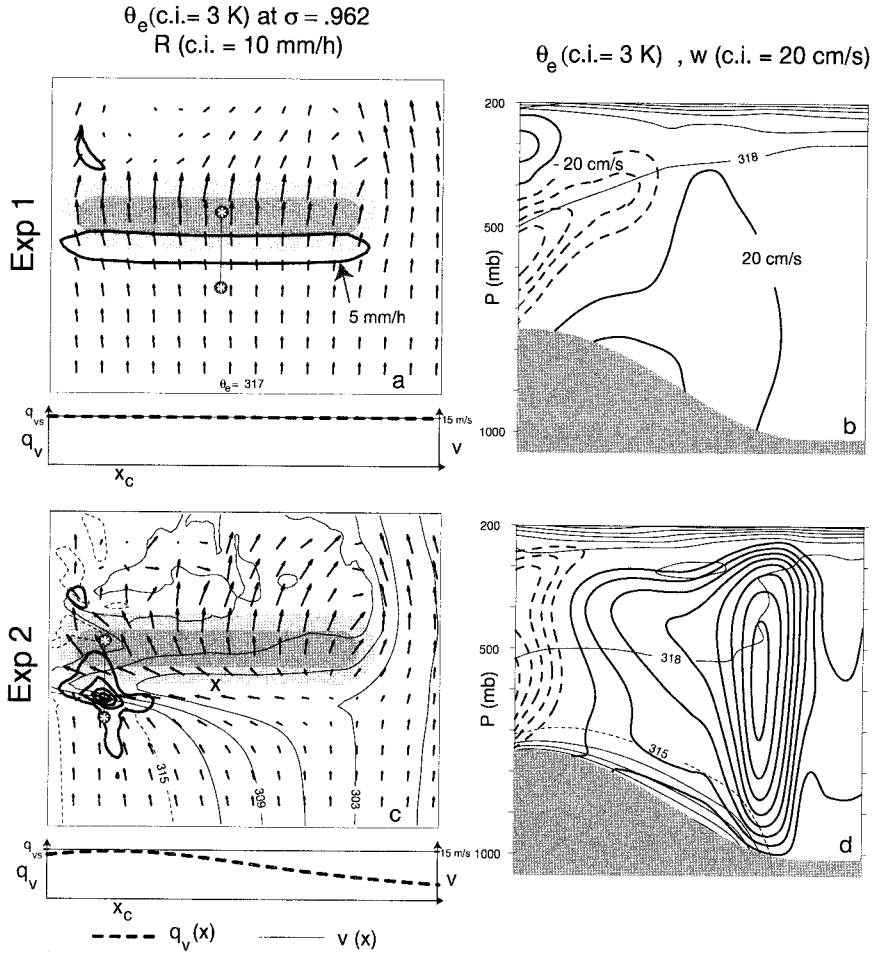

FIG. 14. (a) Rain rate R, θ_e, and horizontal velocity vectors at $\sigma = 0.962$ on the display domain shown in Fig. 13a, and (b) θ_e and w, in the vertical cross sections indicated in (a), of nearly steady (12 h) solutions from experiment 1; (c) and (d) show the same fields for experiment 2 except that the solution at 24 h is exhibited. Initial distribution of $q_v(x)$, $v(x)$ at $z = 0$ is indicated.

than in the dry case (Fig. 12a), there is a weaker relative-vorticity perturbation over the ridge, and consequently, a weaker deflection of the oncoming flow in the moist case (not shown).

Although the foregoing example has limited direct applicability, it serves to strengthen the idea that a reduction in static stability to zero in the part of the flow where condensation is taking place reduces the effective static stability of the entire flow by a much smaller amount. Hence there is some justification for using Fig. 11 as a guide to orographic-flow modification with latent heating, except with V/N increased by at most a factor of two. Hence a mountain of height $H = 1$ km may produce nonlinear response with unsaturated moist-adiabatic airflow and a linear response with saturated moist-adiabatic airflow. Since the abscissa L is logarithmic, an increase of the effective V/N by a factor of two merely signifies a slight increase in the horizontal scale dividing nonhydrostatic and hydrostatic flow regimes. By this reasoning nonhydrostatic effects may be neglected in the present considerations.

d. Hypothesis

The discussion so far of the effect of latent heating on orographic-flow modification serves only to reinforce the prevailing notion that latent-heat release makes the flow response more like the ''quasigeostrophic (QG) weak orog'' icon (flow-over with weak leftward perturbation) than the ''QG strong orog'' icon (flow-around toward the left). However, the simulations discussed in section 3 have aspects of both; for example, the saturated high-θ_e air shown in Figs. 7c,d, and Fig. 8b, flows over a tall barrier, yet suffers a strong leftward deflection. To explain this and other features, we need to augment the simple notions with the following proposition: *The horizontal gradient of saturation deficit is a key factor in determining the orographic-flow modifi-*

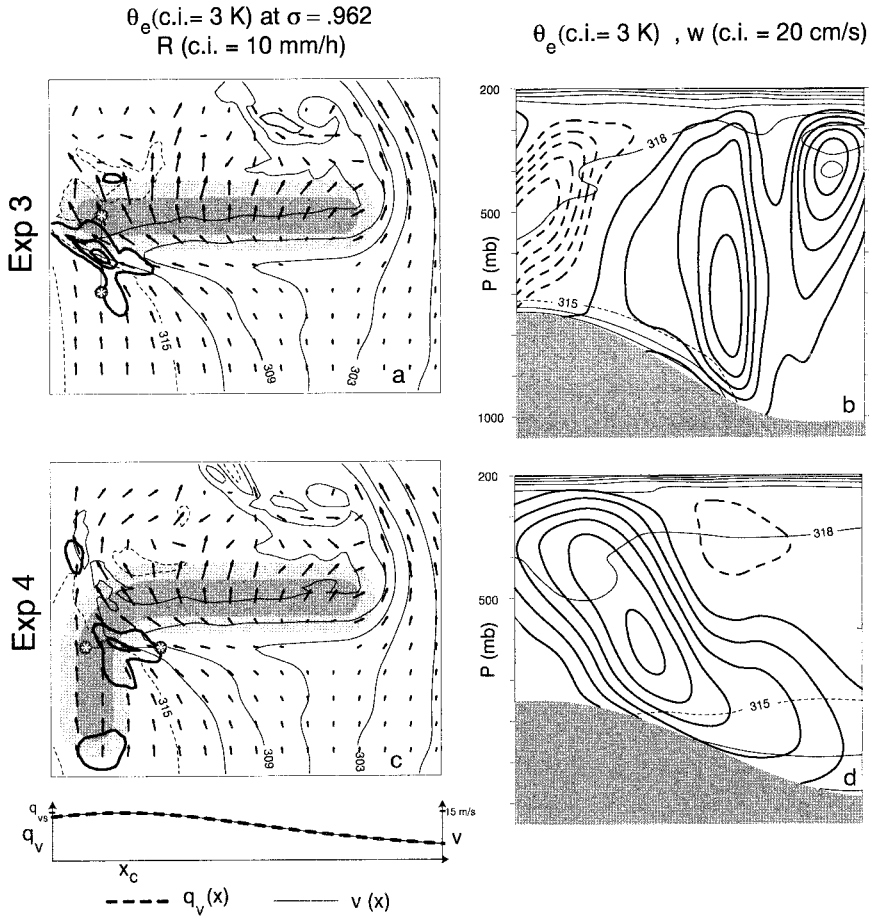

FIG. 15. As in Fig. 14 except for experiments 3 and 4.

cation, and consequently, the orographic control of rainfall.

With this concept one can understand in Fig. 7 why there are flow-over as well as flow-around aspects to the orographic-flow modification. The leftward deflection of the drier air to the east is essential for several reasons. First, it decreases locally the synoptically driven eastward progress of the rain-producing features and so it increases rainfall duration T toward the west end of the idealized Alps (i.e., in Piedmont). [In support of this we note that even the no leg simulation (Fig. 10b) shows a west-end maximum.] The second reason is that the convergence between less-deflected saturated air and more-deflected subsaturated air (Fig. 7c) can apparently produce strong vertical motion (Fig. 8b) and hence a strong rain rate (Fig. 6c). The lack of a direct connection between maximum w and VH/L helps us understand why the less steep simulation (Fig. 10a), with orographic slope H/L 50% that of the ideal Alps, produces only 12% less rain.

The progress beyond the qualitative plausibility of these ideas, we turn next to MM5 simulations again with idealized Alpine barriers, but now also with idealized environmental flows.

5. Simulations with idealized environmental flow

The goal of this section is to put the foregoing more or less qualitative theoretical ideas to a quantitative test. To do this, we configure the MM5 model to run on an f plane ($f = 10^{-4}$ s^{-1}) using a Cartesian grid on a horizontal domain 1000 km $\times$ 1000 km with uniform grid intervals of 10 km as shown in Fig. 13a (the map of Europe is included for reference only). The model domain in the vertical extends to 100 mb and is resolved by 30 unevenly spaced σ levels. Surface stress and heat flux are set to zero, and hence a parameterization of the planetary boundary layer is not used. As in the simulations of section 3, the Kain–Fritsch parameterization is included, but since the idealized flows studied here are all initially moist neutral (Fig. 13b), it plays little role. At the upper boundary a wave-radiation condition is employed as discussed in Dudhia (1993). At the lateral boundaries, the fields are relaxed to the fixed initial conditions over four grid intervals; although this may produce spurious reflections at the outflow boundaries, the features of interest form early enough in the integrations to be considered unaffected by such numerical artifacts. For simplicity there is no radiation or diurnal cycle, and only warm-rain processes are included.

The numerical experiments reported here primarily focus on the effects of an east-west gradient of the ambient water vapor mixing ratio $q_v(x, z)$ with a barotropic southerly wind $v(x)$. No attempt is made here to model the east–west translation of these features and so the emphasis here is necessarily on rain rate R, rather than duration time T, although implications for the latter will be apparent. The orography (3.1) is introduced impulsively at $t = 0$, and the solutions are integrated until a near steady state is reached (12 h unless otherwise mentioned) near the orography.

a. Saturated moist-adiabatic flow incident on an east–west barrier

Based on the discussion of section 4c, the most natural starting point is the investigation of the orographic-flow modification when the ambient southerly wind $v(x) = V$, and $q_v(x, z) = q_{vs}(z)$, where V and the saturation mixing ratio $q_{vs}(z)$ are constant in x.[2] The saturation mixing ratio $q_{vs}(z)$ comes from the sounding shown in Fig. 13b, which is modeled after the one analyzed in the ideal Alps simulation (Fig. 9b). Specifically $q_{vs}(z)$ and $\theta(z)$ were obtained from the moist adiabat originating at (1015 mb, 289 K) extending up to (225 mb, 213 K); from the latter point to the model top (100 mb), we assumed an isothermal atmosphere with the relative humidity approaching 30%. For experiment 1 we let $V = 15$ m s^{-1} and use the same orography as in the no leg simulation (Fig. 10b), except with $L = 120$ km.

Figure 14a shows the nearly steady horizontal flow pattern (with constant θ_e) at the near-terrain-following level $\sigma = 0.962$ together with the rain rate R on the subdomain indicated in Fig. 13a. As conjectured in section 3c, the saturated flow surmounts the obstacle with little deflection; on the other hand, the leeside contains a full suite of nonlinear flow phenomena ranging from a hydraulic jump on the west end [evidenced by the local maximum of R; cf. Fig. 7b of Schneidereit and Schär (2000)] to a downstream shear line on the east end. A north–south vertical cross section of θ_e and w show the strong asymmetry induced by latent heating with rising motion decaying with height on the windward side and strong leeside sinking motion. The maximum rain rate $R_{\max} \approx 9$ mm h^{-1} and occurs along an east–west line near the location of steepest slope and comes entirely from the explicit precipitation physics of the model.

A quantitative estimate of $R_{\max}$ from (4.3) can be made as follows. Numerical calculation of $\rho_{vs}(z)$ from the moist adiabat shown in Fig. 13b shows that

$$\rho_{vs}(z) \approx \rho_{vs}(h) \exp\left(-\frac{z - h}{\lambda_\rho}\right), \tag{5.1}$$

[2] Since geostrophy requires horizontal variation of pressure, q_{vs} actually varies by about 2% across the domain.

TABLE 1. R (mm h^{-1}) vs V (m s^{-1}) and L (km).

V	L	$R_{\text{M M5}}$	$R_{(5.3)}$
10	120	6	6.1
15	120	9	9.2
20	120	12	12.2
15	240	6	6.0
15	60	11	12.3

where $\lambda_\rho \approx 3000$ m. Estimating w from the two-dimensional QG equations of section 4c gives

$$w(z) = V\alpha \exp\left(-\frac{z - h}{\lambda_w}\right), \tag{5.2}$$

where $\lambda_w \equiv 2Lf/N_{\text{eff}}$ and N_{eff} is the effective static stability; the slope $\alpha = \partial_y h$ with maximum $\pi H/2L$ occurring at $y = L/2$, according to (3.1). Substituting (5.1)–(5.2) into (4.3) then gives

$$R = V\alpha\rho_{vs}(h)\frac{\lambda_w}{\lambda_w + \lambda_\rho}, \tag{5.3}$$

which reduces to (4.4) for $\lambda_w \gg \lambda_\rho$ and with $\alpha = H/L$ for a triangular mountain. Since there is a certain amount of arbitrariness in our estimate of λ_w, we choose $N_{\text{eff}} = 0.0075$ s^{-1} to obtain a good fit of the prediction from (5.3) to the result from the MM5 simulation for $V = 15$ m s^{-1} and $L = 240$ km. Table 1 shows $R_{\max}$ as a function of V and L from MM5 and from (5.3) and indicates that the QG scaling for λ_w gives a good estimate of the behavior of $R_{\max}(V, L)$ (for $L \gg 60$ km). This agreement would not have been obtained had we chosen the nonrotating estimate for λ_w ($\sim V/N$).

Simulations using various profiles $v(x)$ and a uniformly saturated initial air mass produced only minor and expected differences (e.g., R is larger where v is larger) from the behavior shown in Table 1 and Figs. 14a,b.

b. Effects of a horizontal gradient of saturation deficit

In experiment 2, all conditions are kept the same[3] except we let

$$q_v(x, z) = q_{vs}(z)\frac{x_s^2}{x_s^2 + (x - x_c)^2}, \tag{5.4}$$

where $x_c = 310$ km (the origin is the lower left-hand corner of the domain shown in Fig. 13a), and $x_s = 450$ km; this profile is motivated by the analysis of the flow from the ideal Alps simulation (Fig. 7).

Figures 14c,d show the results of experiment 2 (run to 24 h to achieve a steady state). Figure 14c shows the

[3] A small change with height of v is introduced by the imposed initial geostrophic balance since (5.4) implies an x gradient of virtual potential temperature; the effect amounts to at most 3 m s^{-1} over the domain depth.

strong leftward deflection of the subsaturated air, this major qualitative change in the horizontal flow structure with respect to the uniformly saturated case (experiment 1) is accompanied by a near quadrupling of $R_{\max}$ to ~40 mm h^{-1}. Consistent with the latter, the vertical cross section shown in Fig. 14d indicates a near quadrupling of $w_{\max}$, which appears as an elevated maximum just above a layer of low-θ_e air flowing out of the cross section. The low-θ_e air, in effect, redefines the shape of the mountain producing a larger slope at a location upstream of the steepest slope of the orography. Note that the low-level blocking begins well to the east of the precipitation location, and therefore, any effect on blocking due to evaporative cooling of precipitation is secondary.

c. Effects of a horizontal gradient of saturation deficit and wind with and without an L-shaped orography

The ideal Alps simulations show that the southerly wind is maximized at the location where the moisture is maximum, hence in experiment 3 we continue to use the profile (5.4) for $q_v(x)$ but also let

$$v(x) = V\frac{x_s^2}{x_s^2 + (x - x_c)^2}, \tag{5.5}$$

with $V = 15$ m s^{-1}. Figures 15a,b show there are few qualitative differences between experiments 2 and 3. Quantitatively, however, experiment 3 reaches a steady state sooner (the 12-h solution is shown) and the rain rate is reduced to ~30 mm h^{-1}. The maximum in w at the upper right-hand (south) side is a transient feature that propagates southward (and is also present at times is experiment 2). Integration for an additional 12 h showed regeneration and southward propagation, but with no significant effect on the lower-level feature producing the heavy rain.

The final experiment (experiment 4) uses the same environment (5.4)–(5.5) as experiment 3, except with the sideways L shape described in section 3b, and used for the experiment less steep (Fig. 10a). Comparing Figs. 15a and 15c shows that the L shape induces little qualitative change in the structure of the rain-producing flow feature on the windward side; quantitatively, $R_{\max} \approx 20$ mm h^{-1} and consistent with the values observed (Fig. 4b) and simulated (Figs. 5c and 6c) during the period of most intense rainfall of the 1994 Piedmont flood. The north–south leg of the sideways L shape induces other quantitative changes such as the placement of $R_{\max}$ on the slope and in the inside corner of the sideways L shape; Fig. 15d shows that $w(z)$ still has an elevated maximum, but is displaced more toward the mountain crest.

In these idealized experiments, the upstream distributions (5.4)–(5.5) are held fixed in time, whereas in the actual case (e.g., Fig. 2) the moist tongue translates eastward over time. It is clearly plausible that the westward flow perturbations shown in Fig. 15a (experiment 3) can have a major effect in retarding the eastward progress of the moist tongue and hence in increasing the rain duration, even without the L shape; evidence for this can be seen in the west-side rainfall maximum obtained in the no leg simulation (Fig. 10b). Experiment 4 shows that for a nontranslating southlerly flow, the leg slightly decreases the local rainfall rate. The main effect of the north–south leg can be seen in the ideal Alps experiment where the leg retards the eastward progress of the cold front (Fig. 7c) and so increases the duration of the rain over Piedmont.

d. Discussion

With the few idealized simulations described here, we believe we can describe the more important rain-producing flow features of the real-data simulations discussed in section 3. The ideal Alps (and CTRL) simulations indicated two stages of orographic rain. In the early stage (0509, Fig. 8a) the moist southerly flow is directly forced upward by the mountain with maximum $w(z)$ decaying with height above the mountain surface; the east–west gradient of moisture is not so pronounced (Fig. 7b) and the rain-producing part of the flow (Fig. 8a) is similar to that shown in experiment 1 (Fig. 14b). In fact, for $V = 12$ m s^{-1} and $L = 60$ km, the simple formula (5.3) gives $R = 9.4$ mm h^{-1}, which can be compared with the ~10 mm h^{-1} from ideal Alps (Fig. 4b) or CTRL (Fig. 5b). In the later stages (0521, Fig. 8b), the moist southerly flow rides over a blanket of low-θ_e air that has been deflected by the east–west portion of the Alpine barrier, similar in fact to what we observe in experiments 2–4; also similar is the fact that the rain rate more than doubles. The simulation with the L-shaped orography and the gradient in saturation deficit produces $R_{\max} \approx 20$ mm h^{-1} (Fig. 14e), which is close to that obtained in ideal Alps (Fig. 5c) and CTRL (Fig. 6c) and in the observations (Fig. 4b).

This second stage of intense rain rate is not predicted by any simple extension of dry orographic-flow theory to the moist case, as none of the simple models discussed in connection with Fig. 11 have an elevated maximum in $w(z)$ on the windward slope. The solution shown in Figs. 14c and 14d is the archetype for the motion associated with saturation deficit increasing eastward; the two basic components of the flow are shown by the three-dimensional time-dependent trajectories from experiment 2 shown in Fig. 16. Figure 16 reinforces the interpretation that the subsaturated, lower-θ_e air is deflected eastward, and undercuts the undeflected saturated, higher-θ_e air. Hence as far as the saturated air is concerned, the mountain shape is effectively changed and the vertical motion depends on the slope of the leading (southern) edge of the low-θ_e blanket (Fig. 14d). The factors that determine the effective mountain shape in these experiments most likely derive from the profiles (5.4)–(5.5) and orographic shape (3.1). Further inves-

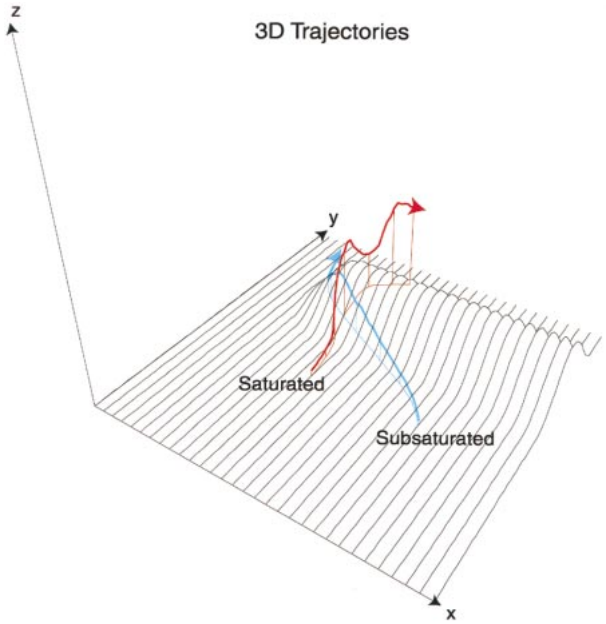

FIG. 16. Trajectories from experiment 2 illustrating how saturated air flows over unsaturated air that has been deflected leftward around the barrier. Trajectories initialized from the flow shown in Fig. 14c and carried forward 12 h; vertical fences connect the trajectories to their respective traces in the $z = 0$ plane. The display domain is the 600 km $\times$ 600 km portion of the computational domain; the vertical scale is four times the actual vertical scale.

tigation of this point is outside the scope of this study (but see the discussion directly below). Suffice it to say that these simulations demonstrate a strong sensitivity of R to the cross-stream saturation deficit.

e. Relation to cold-air damming

The basic flow summarized in Fig. 16 has elements in common with the phenomenon of cold-air damming along the Appalachian Mountains (e.g., Stauffer and Warner 1987). The theoretical model of Xu (1990) considers an infinitely long ridge with neutrally stratified, geostrophically balanced flow across the ridge and a dome of cold air flowing along the ridge. For an infinitely long ridge, the along-ridge geostrophic pressure gradient would continually accelerate the ageostrophic along-ridge flow in the cold dome until the across-ridge Coriolis force would move the cold air up and over the mountain (Pierrehumbert and Wyman 1985). Hence to achieve a steady solution with a cold dome flowing along the upwind slope of the mountain, Xu (1990) includes surface friction in the cold dome to balance the along-ridge geostrophic pressure gradient. In the present case, the ridge is of finite length and so a fluid parcel in the low-θ_e air can accelerate until it reaches the west end of the ridge and then flow north around the obstacle (Fig. 16). The effects of surface friction are undoubtedly important, but it remains for future work to ascertain its role in determining the flow over the cold dome relative to the essentially three-dimensional flow effects envisioned here.

A separate issue concerns the source of the cold air flowing along the mountain ridge. Garner (1999), also within the infinitely long-ridge framework, investigates the effect of a diffuse cross-ridge temperature gradient (in thermal wind balance with an along-ridge wind shear) carried by the across-ridge mean flow and finds that, with temperature decreasing toward the ridge, the baroclinicity allows low-level air to stagnate on the upwind slope of the ridge. In this model the static stability does not vary along the ridge and hence the blocking mechanism is qualitatively different from that discussed here and summarized in Fig. 16. Garner (1999) briefly considers the effect of a weak unbalanced temperature gradient in the along-ridge direction (with colder air on the right, facing with the mean flow) together with the across-ridge temperature gradient and remarks on the enhancement of the upwind cold pool due to cold advection along the ridge (p. 1504). In the present case, we have only the along-ridge baroclinicity due to a small along-ridge variation of θ_v in the mean flow. The main contributor to the flow summarized in Fig. 16 is the along-ridge variation of the degree of saturation, which produces a along-ridge variation in the ability of the mountain to block the flow.

6. Summary and outlook

We have revisited here the 1994 Piedmont flood in an attempt to discover more precisely the mechanism(s) for the intense rainfall. A close look at the radar estimates of precipitation over time (section 2) and numerical simulations with idealized orography (section 3) suggest two different regimes of orographic rain occurred. In the first regime there was simple orographic uplift occurring under nearly moist neutral conditions. The maximum rain rate is directly tied to the maximum vertical velocity, which in turn is directly related to the strength of the flow toward, and the slope of, the mountain barrier. In the second regime there is a more complex orographic response in which variations in the orographic-flow response *along* the mountain barrier set up a pattern of convergence that produced much stronger vertical motion, which is not in general colocated with the steepest mountain slope.

The latter effect is due to the effect of latent-heat release on static stability. Previous sensitivity studies showed the primary importance of latent heating in allowing the moderate southerly flow ($\sim$15 m s^{-1}) to surmount the tall ($\sim$3 km) Alpine barrier and hence produce rain in Piedmont. As a corollary to this idea, we show here that subsaturated air to the east of the saturated stream is fully blocked by the Alps, and owing to the large scale of the Alps, flows westward toward the saturated stream, producing convergence between the two streams in the general vicinity of Piedmont. Simplified calculations with MM5 (section 5) show that

an eastward increase in saturation deficit can produce a large increase in local rain rate.

In our previous paper FLR speculated on the role of the westward flow deflection in the production of rain in Piedmont, since it was considered important for understanding the location and duration of the rainfall. FLR offered two speculations on the source of the eastward flow: one being the mechanism described in this paper, while the other attributed westward wind perturbations in the Po Valley to a small-scale cyclonic circulation that forms over the western Po Valley (see Fig. 15 of FLR). This vortex is associated with the vorticity of the cold front, which, upon close analysis of the ideal Alps simulation (see Fig. 7c), is not directly related to the flow features that produce the intense rain rates. Hence, we now view the vortex as a feature of the cold front's passage from west to east of the Alps, which may contribute to easterly flow perturbations in the Po Valley, but whose existence is not essential for intense Alpine rainfall.

The present study of the mechanisms responsible for intense rain leading to the 1994 Piedmont flood adds to the collection of simple concepts needed to comprehend an immensely complex reality. We are currently analyzing data from the recently completed field phase of the Mesoscale Alpine Programme (MAP; see Bougeault et al. 2001) armed with this extended collection of ideas.

Acknowledgments. We gratefully acknowledge C. Davis for his help with the simplified MM5 simulations discussed in section 5, and D. Muraki and C. Epifanio for their help in constructing the regime diagram shown in Fig. 11. Visitor support for RF came from the Mesoscale and Microscale Meteorology Division of NCAR and a cooperative agreement between the University Corporation for Atmospheric Research and il Ministero della Universita'e Ricerca Scientifica. We would like to thank II Parco Scientifico e Technologico Abruzzo for supplying data from the European Centre for Medium-Range Weather Forecasts. Finally we thank those responsible for the Mesoscale Alpine Programme data archive from which were taken the rain and radar data discussed herein.

REFERENCES

Barcilon, A., J. C. Jusem, and P. G. Drazin, 1979: On the two-dimensional hydrostatic flow of a stream of moist air over a mountain ridge. *Geophys. Astrophys. Fluid Dyn.,* **13,** 125–140.

Benzi, R., M. Fantini, R. Mantovani, and A. Speranza, 1997: Orographic cyclogenesis in a saturated atmosphere and intense precipitation: Baroclinic model solutions under the joint action of localized humidity and mountains. *Ann. Geofis.,* **40,** 1579–1590.

Binder, P., and Coauthors, 1996: MAP—Mesoscale Alpine Programme design proposal. MAP Programme Office, 77 pp. [Available from MAP Programme Office, c/o Swiss Meteorological Institute, Krähbühlstrasse 58, CH-8044 Zürich, Switzerland.]

Bougeault, P., and Coauthors, 2001: The MAP Special Observing Period. *Bull. Amer. Meteor. Soc.,* **82,** 433–462.

Buzzi, A., and S. Tibaldi, 1977: Inertial and frictional effects on rotating and stratified flow over topography. *Quart. J. Roy. Meteor. Soc.,* **103,** 135–150.

——, N. Tartaglione, and P. Malguzzi, 1998: Numerical simulations of the 1994 Piedmont flood: Role of orography and moist processes. *Mon. Wea. Rev.,* **126,** 2369–2383.

Doswell, C. A., C. Ramis, R. Romero, and S. Alonso, 1998: A diagnostic study of three heavy precipitation episodes in the western Mediterranean region. *Wea. Forecasting,* **13,** 102–124.

Dudhia, J., 1993: A nonhydrostatic version of the Penn State–NCAR Mesoscale Model: Validation tests and simulation of an Atlantic cyclone and cold front. *Mon. Wea. Rev.,* **121,** 1493–1513.

Durran, D. R., and J. B. Klemp, 1983: A compressible model for the simulation of moist mountain waves. *Mon. Wea. Rev.,* **111,** 2341–2361.

Fantini, M., 1995: Moist Eady waves in a quasigeostrophic three-dimensional model. *J. Atmos. Sci.,* **52,** 2473–2485.

Ferretti, R., S. Low-Nam, and R. Rotunno, 2000: Numerical simulations of the Piedmont flood of 4–6 November 1994. *Tellus,* **52A,** 162–180.

Garner, S. T., 1999: Blocking and frontogenesis by two-dimensional terrain in baroclinic flow. Part I: Numerical experiments. *J. Atmos. Sci.,* **56,** 1495–1508.

Joss, J., and Coauthors, 1998: *Operational Use of Radar for Precipitation Measurements in Switzerland.* VDF Hochschulverlag AG an der ETH, 108 pp.

Kain, J. S., and J. M. Fritsch, 1993: Convective parameterization for mesoscale models: The Kain–Fritsch scheme. *The Representation of Cumulus in Numerical Models, Meteor. Monogr.,* No. 46, Amer. Meteor. Soc., 165–177.

Kessler, E., 1969: *On the Distribution and Continuity of Water Substance in Atmospheric Circulation, Meteor. Monogr.,* No. 32, Amer. Meteor. Soc., 84 pp.

Merkine, L.-O., and E. Kalnay-Rivas, 1976: Rotating stratified flow over finite isolated topography. *J. Atmos. Sci.,* **33,** 908–922.

Peng, M. S., S.-W. Li, S. W. Chang, and R. T. Williams, 1995: Flow over mountains: Coriolis force, transient troughs and three dimensionality. *Quart. J. Roy. Meteor. Soc.,* **121,** 593–6113.

Pierrehumbert, R. T., and B. Wyman, 1985: Upstream effects of mesoscale mountains. *J. Atmos. Sci.,* **42,** 977–1003.

Queney, P., 1948: The problem of air flow over mountains: A summary of theoretical studies. *Bull. Amer. Meteor. Soc.,* **29,** 16–26.

Romero, R., C. Ramis, S. Alonso, C. A. Doswell, and D. J. Stensrud, 1998: Mesoscale model simulations of three heavy precipitation events in the western Mediterranean region. *Mon. Wea. Rev.,* **126,** 1859–1881.

Schneidereit, M., and C. Schär, 2000: Idealised numerical experiments of alpine flow regimes and southside precipitation events. *Meteor. Atmos. Phys.,* **72,** 233–250.

Smith, R. B., 1979: The influence of mountains on the atmosphere. *Advances in Geophysics,* Vol. 21, Academic Press, 87–230.

Smolarkiewicz, P. K., and R. Rotunno, 1989: Low Froude number flow past three-dimensional obstacles. Part I: Baroclinically generated lee vortices. *J. Atmos. Sci.,* **46,** 1154–1164.

Stauffer, D. R., and T. T. Warner, 1987: A numerical study of cold-air damming and coastal frontogenesis. *Mon. Wea. Rev.,* **115,** 799–822.

Steinacker, R., 1981: Analysis of the temperature and wind field in the Alpine region. *Geophys. Astrophys. Fluid. Dyn.,* **17,** 51–62.

Troen, I., and L. Mahrt, 1986: A simple model of the atmospheric boundary layer; sensitivity to surface evaporation. *Bound.-Layer Meteor.,* **37,** 129–148.

Trüb, J., and H. C. Davies, 1995: Flow over a mesoscale ridge: Pathways to regime transition. *Tellus,* **47A,** 502–524.

Xu, Q., 1990: A theoretical study of cold air damming. *J. Atmos. Sci.,* **47,** 2969–2985.